Engineering Highly Vascularized Bone Tissues by 3D Bioprinting of Granular Prevascularized Spheroids

Article *in* ACS Applied Materials & Interfaces · September 2023

DOI: 10.1021/acsami.3c08550

11 authors, including:

Fang Yongcong
Tsinghua University
30 PUBLICATIONS **434** CITATIONS
SEE PROFILE

Bingyan Wu
Tsinghua University
3 PUBLICATIONS **12** CITATIONS
SEE PROFILE

Ting Zhang
Tsinghua University
52 PUBLICATIONS **1,458** CITATIONS
SEE PROFILE

Wei Sun
IMS Health
236 PUBLICATIONS **10,783** CITATIONS
SEE PROFILE

ACS APPLIED MATERIALS & INTERFACES

www.acsami.org

Research Article

Engineering Highly Vascularized Bone Tissues by 3D Bioprinting of Granular Prevascularized Spheroids

Yongcong Fang, Mengke Ji, Bingyan Wu, Xinxin Xu, Ge Wang, Yanmei Zhang, Yingkai Xia, Zhe Li, Ting Zhang, Wei Sun, and Zhuo Xiong*

Cite This: https://doi.org/10.1021/acsami.3c08550

Read Online

ACCESS | Metrics & More | Article Recommendations | Supporting Information

ABSTRACT: The convergence of 3D bioprinting with powerful manufacturing capability and cellular self-organization that can reproduce intricate tissue microarchitecture and function is a promising direction toward building functional tissues and has yet to be demonstrated. Here, we develop a granular aggregate-prevascularized (GAP) bioink for engineering highly vascularized bone tissues by capitalizing on the condensate-mimicking, self-organization, and angiogenic properties of prevascularized mesenchymal spheroids. The GAP bioink utilizes prevascularized aggregates as building blocks, which are embedded densely in extracellular matrices conducive to spontaneous self-organization. We printed various complex structures with high cell density (~1.5 × 10^8 cells/cm^3), viability (~80%), and shape fidelity using GAP bioink. After printing, the prevascularized mesenchymal spheroids developed an interconnected vascular network through angiogenic sprouting. We printed highly vascularized bone tissues using GAP bioink and found that prevascularized spheroids were more conducive to osteogenesis and angiogenesis. We envision that the design of the GAP bioink could be further integrated with human-induced pluripotent stem cell-derived organoids, which opens new avenues to create patient-specific vascularized tissues for therapeutic applications..

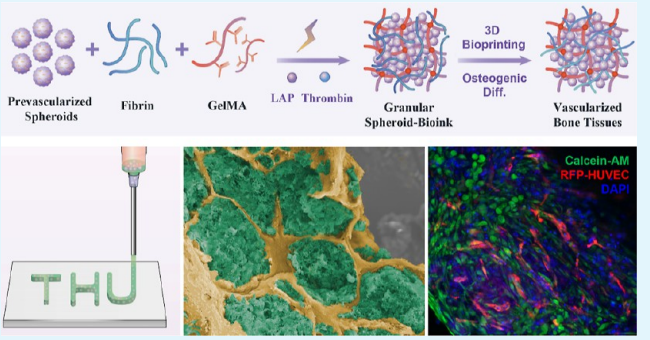

KEYWORDS: *3D bioprinting, condensation, vascularization, organoids, tissue engineering*

1. INTRODUCTION

Three-dimensional (3D) bioprinting is widely applied in regenerative medicine due to its powerful ability to control the spatial deposition of cells and biomaterials.[1] However, it is challenging to reproduce the intricate microarchitecture, cell-type composition, and function of native tissues by printing individual cells at the appropriate place due to the printing resolution (~100 μm).[2] Recently, the field of regenerative medicine has evolved toward a new concept of "in vitro biomimicry of in vivo tissue development".[3] Much effort has been devoted to engineering the process of in vitro tissue development rather than the target tissues with knowledge from developmental biology.[4] During embryonic development and regeneration, condensation as a result of stem cell aggregation occurs and initiates cell differentiation and morphogenesis in virtually every organ in the human body.[5] For example, mesenchymal cell condensation is considered the major event that initiates mesenchymal commitment to the osteogenic and chondrogenic lineages.[6] Previous studies have shown that cell condensation into spheroids triggers the in vitro differentiation of human mesenchymal stem cells (MSCs) into osteocyte-like cells,[7] indicating a critical role of cell condensation in morphogenetic processes.

Engineering the organization and fusion of multicellular aggregates, such as spheroids and organoids, represents a biomimetic cell assembly process fundamental to in vitro tissue and organ development.[8] In this regard, cell aggregates with intensive cell−cell contacts and dense extracellular matrix (ECM) are more favorable components for conventional bioinks than dispersive cells.[9] Thus, various approaches have been developed for assembling these multicellular aggregates into physiologically relevant tissues, mimicking their native counterparts.[10] By using the Kenzan[11] or aspiration-assisted bioprinting strategy,[12] individual spheroids can be assembled into macroscale tissues with high positional accuracy; however, the "pick-and-place" approach is inherently slow, making it unsuitable for large-scale tissue fabrication.[13] Using a micromolding technique, the geometric confinement led to the fusion of the spheroids, resulting in a dense tissue construct

Received: June 14, 2023
Accepted: August 31, 2023

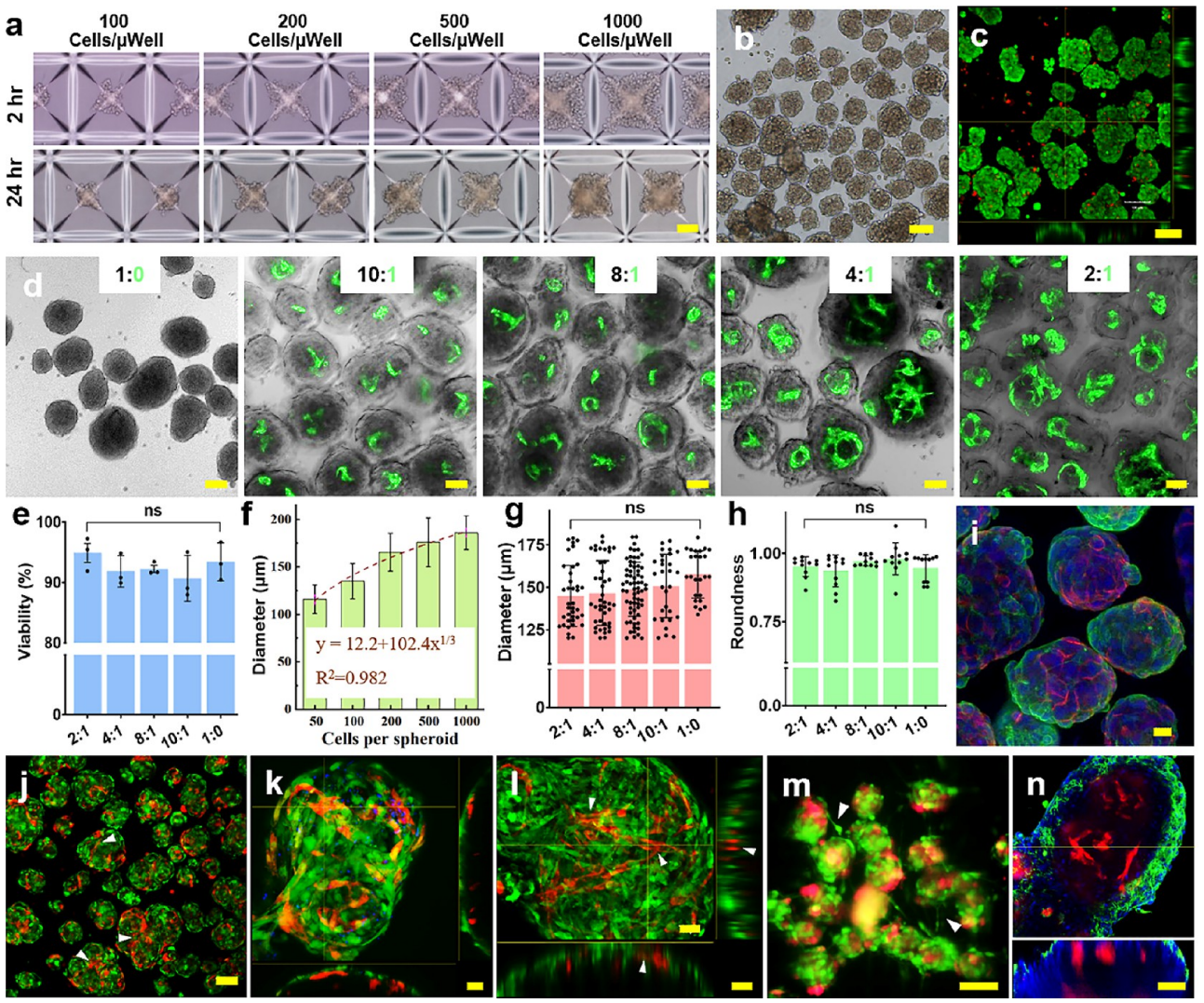

Figure 1. Large-scale production and characterization of prevascularized spheroids. (a) Formation of spheroids at different seeding densities at 2 and 24 h. (b) Optical image of harvested MSC spheroids after 3 d. (c) Confocal live/dead image of MSC spheroids (Calcein-AM: green, PI: red). (d) Morphology of multicellular spheroids (HUVECs: green). (e) Viability comparison of multicellular spheroids at various cell ratios of MSCs and HUVECs. (f) Relationship between spheroid diameters and seeding densities. The dotted brown line indicates the fitted curve of the relationship between spheroid diameters and seeding densities. (g,h) Diameter and roundness measurement of multicellular spheroids. (i) Immunostaining of MSC/HUVEC spheroids (CD44: green, CD31: red, cell nuclei: blue). (j) Confocal image of prevascularized spheroids consisting of GFP-MSCs and RFP-HUVECs. The white arrows denote spheroid fusion into larger aggregates. (k,l) 3D reconstruction showing capillary formation within spheroids. The white arrows denote the cord-like structures formed by the self-assembly of HUVECs. (m,n) Confocal images of prevascularized spheroids embedded in a 3D fibrin gel on day 1 (m) and day 7 (n). The white arrows denote the cell migration of prevascularized spheroids into the surrounding fibrin matrix (MSC: green, HUVEC: red, cell nuclei: blue). Scale bars in (a−c) 100 μm; (d) 50 μm; (i) 20 μm; (j) 100 μm; (k) 10 μm; (l) 50 μm; (m) 200 μm; (n) 50 μm. One-way ANOVA was used to analyze the data, "*" indicates statistical significance ($*p < 0.05$), and ns indicates no significance.

with relatively simple architectural features.[14] As an alternative, acoustic[15] and magnetic fields[16] have been used to drive the patterning and fusion of spheroids to yield functional tissue constructs. It is noteworthy that spheroid fusion often results in morphogenesis as well as significant changes in shape that are difficult to predict.[17] This is due to the complex interactions between the spheroids, which are not fully understood.[18] As a result, such field-based approaches are limited to structures of low complexity. This limitation is further compounded by the fact that the spheroid fusion process is inherently slow.[19] In a recent study, Goulart and colleagues developed a bioink containing spheroids that can be used to print hepatic tissues;[20] however, encapsulating only a relatively low concentration of spheroids inhibited the ability of the spheroids to organize.[21] This lack of organization resulted in a poor representation of the hepatic lobule architecture.

In the absence of vasculature, tissue constructs formed by spheroid fusion often have difficulty scaling up to viable thick tissues beyond the millimeter scale and thus cannot replicate the macroscopic architecture of native solid organs.[22] To introduce vasculature into thick tissue constructs, Skylar-Scott et al.[23] recently developed the sacrificial writing into functional tissue (termed SWIFT) technique to support the bioprinting of embedded vascular networks to ensure tissue viability by leveraging densely packed spheroids as a suspension bath. The SWIFT strategy can only produce bulk tissues with a vascular network since the tissue constructs are not 3D printed but cast

https://doi.org/10.1021/acsami.3c08550
ACS Appl. Mater. Interfaces XXXX, XXX, XXX−XXX

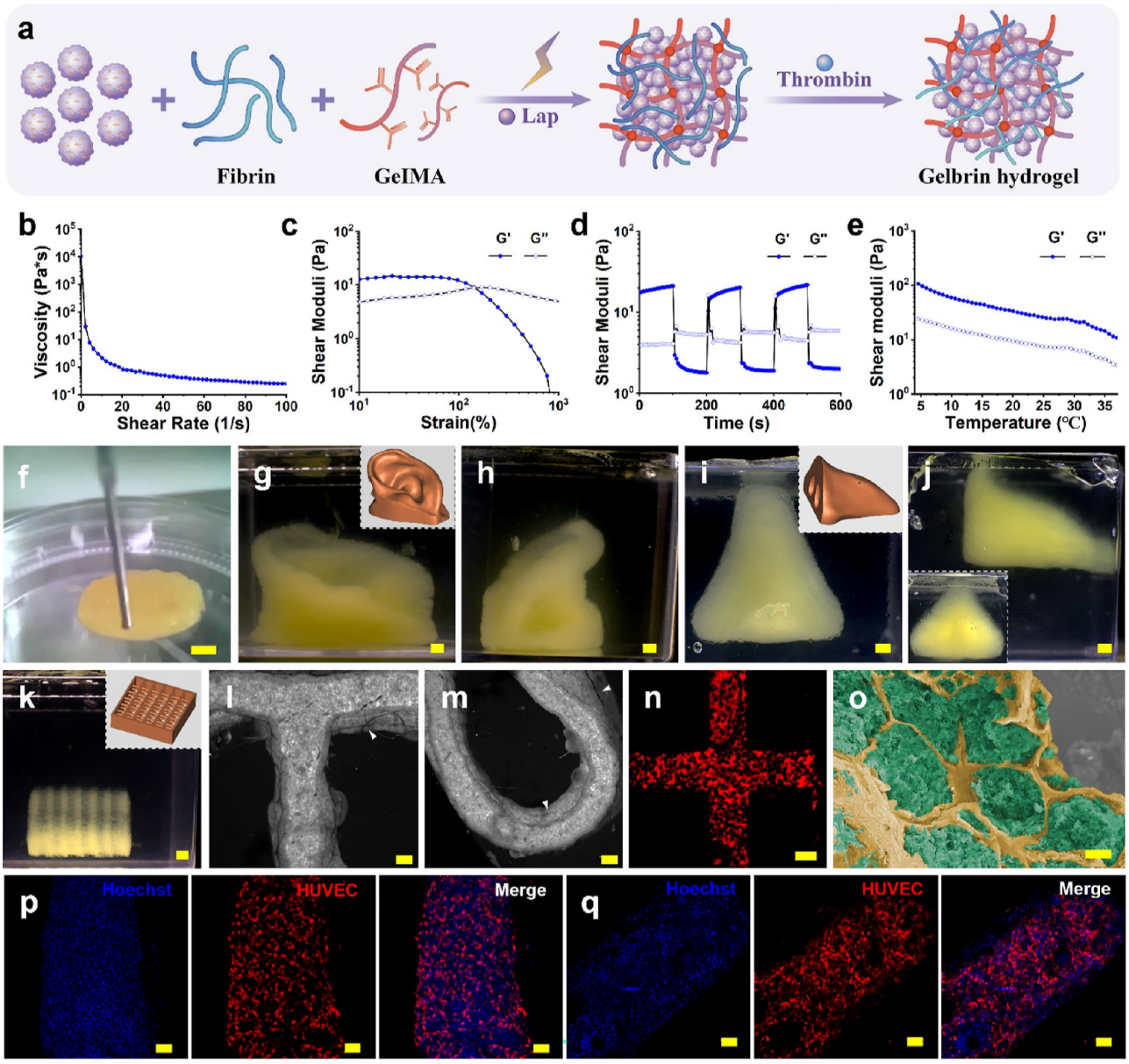

Figure 2. 3D bioprinting and characterization of GAP bioink. (a) Schematic diagram for the composition of GAP bioink. (b–e) Rheological characterization showing shear thinning (b), strain yielding (c), self-healing properties (d), and a wider temperature window for 3D bioprinting (e). (f) 3D bioprinting of a circular construct using GAP bioink. (g–k) 3D bioprinting of an ear model (g,h), nose model (i,j), and multilayer lattice (k) in a suspension medium (inset on the top right: 3D CAD model). (l,m) Fluorescent images of the printed constructs. The white arrows denote the fusion between adjacent layers. (n) Magnified fluorescent image of a 3D printed lattice structure. The red channel denotes the hydrogel, while spheroids are not shown. (o) SEM image showing a honeycomb-like structure of the printed structure. (p,q) 3D printed structures consisting of prevascularized spheroids on day 1 (p) and day 7 (q) (HUVECs: red; cell nuclei: blue). Scale bars are in (f) 2 mm; (g–k) 2 mm; (l–n) 500 μm; (o) 20 μm; and (p,q) 100 μm.

using a custom mold. The thick tissue constructs maintained high viability through perfusion of the printed vascular network; however, capillaries at the size of several microns are too small to be printed by SWIFT. Capillaries in vivo provide an efficient exchange of nutrients and oxygen[24] as well as beneficial effects on cell-specific functions.[25] In previous studies, vessel-forming cells have been incorporated into multicellular aggregates to generate prevascularized spheroids for regenerative applications.[26] In a recent study, De Moor et al. demonstrated that prevascularized spheroids can be encapsulated within the GelMA hydrogel for 3D bioprinting.[27] However, prevascularized spheroids were merely used as supplementary materials with relatively low concentrations, which significantly limited spheroid fusion and tissue remodeling rather than as primary vascularization units for bioprinting physiologically relevant tissues with high cell density and vascularity.

To address this challenge, we report a novel design of a granular-aggregate-prevascularized (GAP) bioink to leverage prevascularized spheroids for the 3D bioprinting of vascularized complex tissue constructs. The GAP bioink consists of two phases, namely, densely packed prevascularized aggregates that occupy the major space as discrete phases and an ECM solution that integrates the aggregates in a robust manner. As a result of the granular nature of the cell aggregates, the GAP bioink behaves like classic jammed microgel bioinks with the

https://doi.org/10.1021/acsami.3c08550
ACS Appl. Mater. Interfaces XXXX, XXX, XXX−XXX

necessary viscoelastic, shear thinning, and shear-recovery properties for extrusion bioprinting. Printing parameters and aggregate content were optimized to balance printability and fusion capabilities, resulting in high cell density and satisfactory viability postprinting. We demonstrated that the condensation condition and angiogenic capabilities of the GAP bioink accelerated the vascularization and osteogenesis processes. This strategy provides a more efficient method of printing dense complex tissues with intricate vascular networks, which have great potential for bone and tissue regeneration.

2. RESULTS AND DISCUSSION

In this study, MSCs were used for their capability to differentiate into multiple lineages.[28] For the large-scale production of MSC spheroids, we used commercially available AggreWell 400EX plates (StemCell Technologies) with inverse pyramidal-shaped microwells. MSC spheroids self-assembled and compacted after 24 h (Figure 1a). The poor cell−substrate adhesion allowed facile harvesting of the intact MSC spheroids with a regular round shape and reproducible size on day 3 (Figure 1b). Live/dead staining revealed that the culture and harvest process was minimal to the cell viability of MSC spheroids (Figure 1c). The spheroids appeared to be hollow mainly due to the inability of fluorescent dye to penetrate the dense outer cell layers, as previously reported.[29] MSCs have been widely reported to facilitate the formation of capillary networks by human umbilical vein endothelial cells (HUVECs).[30] Therefore, we generated prevascularized spheroids by coculturing MSCs with HUVECs. The ratio between MSCs and HUVECs was optimized at 2:1 to generate a higher extent of capillary formation (Figure 1d). Notably, HUVECs alone failed to form compact spheroids and completely disintegrated during culture (Figure S1). Despite the shear stress during pipetting, these spheroids maintained very high viability (>95%) during culture (Figure 1e). The spheroid sizes were easily adjustable by changing the seeding densities (Figure 1f). The harvested MSC spheroids with 200 cells were characterized as having a narrow size distribution with diameters of 145 ± 18 μm and roundness of 0.87 ± 0.04 (Figure 1g,h). While smaller spheroids would enable higher-feature resolution of 3D bioprinting, the volume of the spheroids generated decreases significantly as d^3 for a fixed number of microwell arrays. Therefore, spheroids containing 200 cells were routinely used in the following experiments.

Immunostaining analysis for platelet endothelial cell adhesion molecule 1 (PECAM-1 or CD31) and CD44 (cluster of differentiation 44) confirmed a dense organization of the MSCs and HUVECs (Figures 1i, S2), in line with a previous report.[22] To visualize microvessel formation, we used prevascularized spheroids containing red fluorescent protein-expressing HUVECs (i.e., RFP-HUVECs) and green fluorescent protein-expressing MSCs (i.e., GFP-MSCs). Spheroid fusion occurred within less than 12 h under rotational culture, indicating a high level of self-organization (Figure 1j). Confocal images showed vessel anastomosis by spheroid fusion to form an interconnected vascular network (Figure 1k,l). Due to its natural presence in humans and FDA approval, fibrin gel has been widely used in regenerative medicine.[31] By encapsulating the MSCs and HUVECs within the fibrin hydrogel (10 mg/mL), we successfully generated extensive capillary-like networks (Figure S3). Similarly, we observed the cell migration of prevascularized spheroids into the surrounding fibrin matrix within 24 h (Figure 1m). On day 7, angiogenic sprouting and vessel formation occurred (Figure 1n); however, the fibrin hydrogel shrank substantially and was compacted into a crinkled structure as a result of cell spreading-induced forces and fibrinolysis, consistent with previous reports.[32]

The encouraging results motivated us to explore using prevascularized spheroids as regenerative units that can be further scaled up to print dense vascularized tissues. Although the fibrin matrix is highly conducive to tissue remodeling and morphogenesis,[33] fibrin and its prepolymer form (fibrinogen) are notoriously known as burdensome candidates for 3D bioprinting.[34] As a result, we developed an ECM solution comprising gelatin−methacryloyl (GelMA) and fibrinogen (termed Gelbrin), in which the GelMA hydrogel rendered the printability of fibrinogen and tuned the physiological and mechanical properties of the Gelbrin composite hydrogel. To leverage the unique self-organization potential of prevascularized aggregates, we prepared the GAP bioink by densely packing these aggregates via centrifugation and mixing them with the Gelbrin solution (Figures 2a, S4). For MSC spheroids with a diameter of 145 ± 18 μm, we used a 21G syringe needle at 21G (inner diameter: 510 μm) with an appropriate nozzle-to-spheroid diameter ratio of ∼3.5. Generally, a smaller nozzle would increase printing fidelity if extrudable;[35] however, a smaller opening of the printing nozzle results in higher stress that significantly reduces cell viability and causes the rupture of spheroids.[36] Therefore, there is a trade-off between printing fidelity and cell viability that must be considered in terms of printing parameters. The compacted spheroids were mixed with Gelbrin solution to produce the GAP bioink at various volume fractions of spheroids (VFS), including 40, 60, and 80%. By comparing the cell viability and cell densities after extrusion, we used GAP bioink with VFS at 60% for the following experiments, which exhibited a cell density of ∼1.5 × 10^8 cells/cm^3 and a viability of ∼80% under optimized conditions (Figure S5).

GAP bioink displayed the requisite shear-thinning (Figure 2b), strain-yielding (Figure 2c), and self-healing properties (Figure 2d), protecting cells from high shear wall stresses during printing and maintaining structural stability after printing. Gelbrin bioink was highly temperature-sensitive because of the sol−gel transition property of the GelMA hydrogel (Figure S6a); however, due to the jammed nature of GAP bioink, its temperature sensitivity was reduced, resulting in a wider extrusion bioprinting temperature window between 15 and 30 °C (Figure 2e). We successfully printed a circular construct (Figure 2f) with smooth extrusion and high fidelity by matching the printing speed and extrusion rate, followed by photo-cross-linking of GelMA (Figure S6f) and enzymatic cross-linking of fibrinogen with a thrombin solution. It is often challenging for conventional extrusion bioprinting to fabricate human anatomical structures encompassing complex geometrical features (e.g., overhangs and cavities).[37] By incorporating a Carbopol-based suspension bath, we successfully printed an ear model (Figure 2g,h), nose model (Figure 2i,j), and multilayer lattice (Figure 2k) with high fidelity. The printed constructs displayed good filament adhesion between adjacent layers (Figure 2l,m) to ensure mechanical stability. To visualize the granular morphology of the 3D bioprinted filaments, we prelabeled the MSC spheroids with green fluorescence and the Gelbrin precursor solution with red fluorescence. Fluorescent images (Figure 2n) of a printed lattice structure showed that spheroids were densely packed

https://doi.org/10.1021/acsami.3c08550
ACS Appl. Mater. Interfaces XXXX, XXX, XXX−XXX

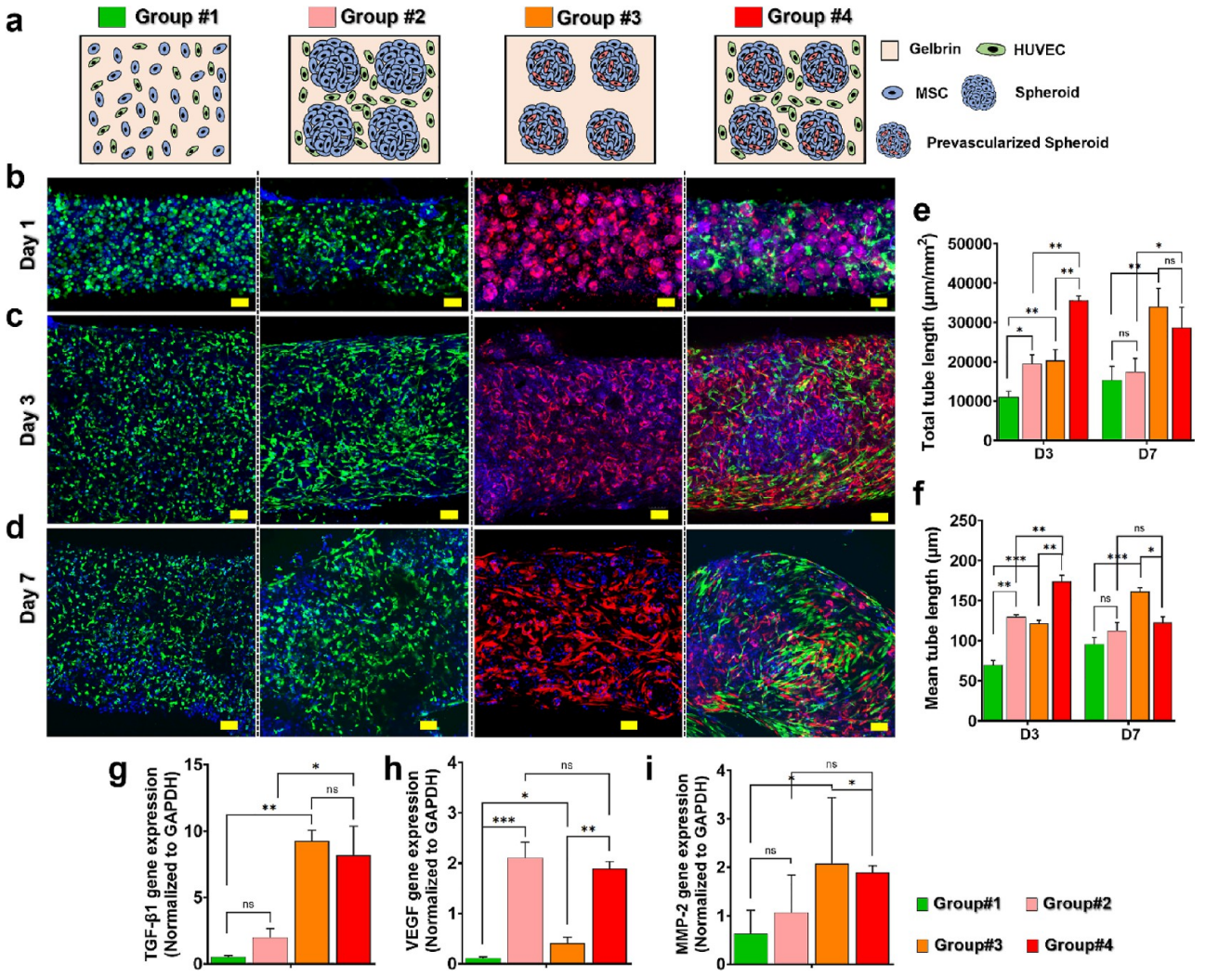

Figure 3. Vasculogenic evaluation of GAP bioink. (a) Illustration of four types of bioinks. (b–d) Confocal images of the printed structures on day 1 (b), day 3 (c), and day 7 (d). (e,f) Quantitative analysis of vascular tube formation after 3 and 7 days in culture. (g–i) Comparative analysis of the mRNA expression of genes involved in angiogenesis-related processes on day 7. Scale bars in parts (b–d) are 100 μm. Student's *t*-test was used to analyze the data, "*" indicates statistical significance (*$p < 0.05$; **$p < 0.01$; ***$p < 0.005$), and ns indicates no significance.

and separated by the surrounding Gelbrin matrix, as confirmed by the scanning electron microscopy (SEM) image (Figure 2o). The honeycomb-like structure of the GAP bioink is highly beneficial for cell–cell contact and tissue remodeling. The prevascularized spheroids formed capillary-like networks on day 1 after printing (Figure 2p). We observed angiogenic sprouting from these spheroids on day 7 (Figure 2q), suggesting that the Gelbrin matrix provides a soft microenvironment that facilitates cell fusion and reorganization, similar to in vivo tissue remodeling and morphogenesis. The mechanical requirements for the regeneration of native bone, particularly load-bearing bone, should be taken into consideration. The GAP bioink had a lower elastic modulus (14.3 ± 2.5 kPa) than the Gelbrin bioink (128.3 ± 7.2 kPa) due to its high cell density (Figure S7a,b). The GAP bioink-printed constructs can be repeatedly compressed at 60% strain many times, whereas Gelbrin fatigued at a 52% strain (Figure S7c,d), suggesting its ability to maintain structural integrity through flexible deformation at the defect site. It is noteworthy that the printed tissue constructs produced by the GAP bioink alone cannot match the mechanical performance of bone tissue in vivo. In future experiments, mechanical matching with bone tissue in vivo can be achieved by coprinting the high-strength synthetic polymer, such as poly caprolactone and polylactic acid, as a supporting framework as previously reported.[38−42]

The rapid and sufficient vascularization of the 3D bioprinted tissue constructs is essential to ensure the optimal cell survival and integration in vivo for large-scale tissues.[43] Furthermore, vascularization plays a key role in bone healing, in both natural and artificial bone implants.[44] Therefore, we further explored the vasculogenic and angiogenic potential of the GAP bioinks by comparing them with conventional dispersive cell-laden (DCL) bioinks in the context of extrusion bioprinting. Conventional DCL bioink containing dispersive MSCs and GFP-HUVECs at a density of 7.5×10^6 cells/cm^3 was used as a control (group #1) since the typical cell density suitable for 3D bioprinting is $(0.1–10) \times 10^6$ cells/cm^3. Three groups of MSC-/HUVEC-laden GAP bioinks were used to examine the effects of prevascularization of spheroids and HUVEC inclusion on tissue vascularization (Figure 3a). GAP bioinks comprising MSC spheroids/GFP-HUVECs (group #2), MSC&RFP-HUVEC spheroids (group #3), and MSC&RFP-HUVEC spheroids/GFP-HUVECs (group #4) were printed and cultured for 7 d in an MSC growth medium (GM)/

https://doi.org/10.1021/acsami.3c08550
ACS Appl. Mater. Interfaces XXXX, XXX, XXX−XXX

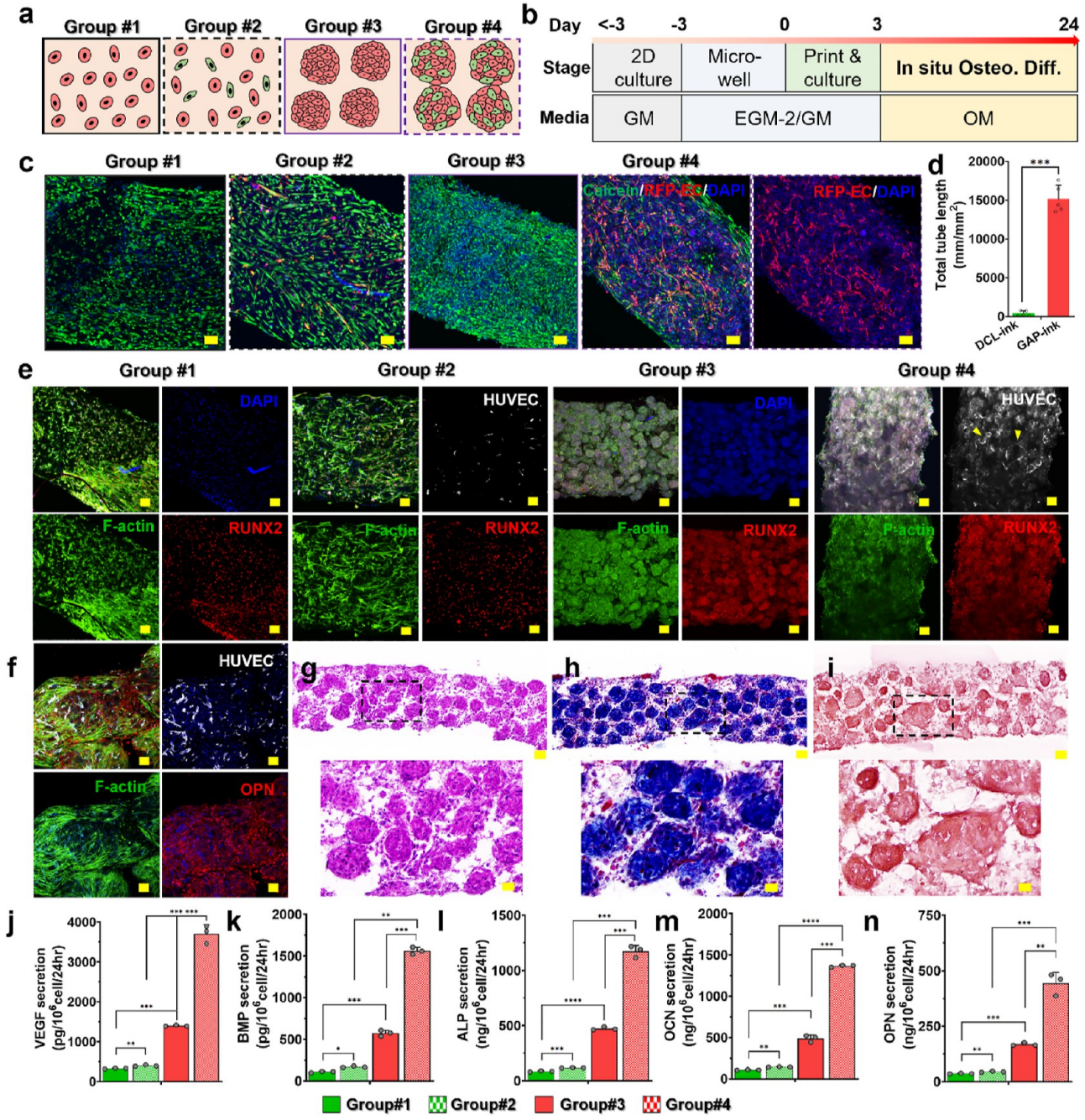

Figure 4. 3D bioprinting of vascularized bone tissues using the vasculogenic and osteogenic GAP bioink. (a) Illustration of four types of bioinks. (b) In vitro osteodifferentiation protocol. (c) Confocal images of the printed structures on day 7 (Calcein-AM: green; HUVEC: red; cell nuclei: blue). (d) Quantitative analysis of vascular tube formation on day 7. (e) Immunofluorescence staining on day 17 (F-actin: green, RUNX2: red, HUVEC: white, cell nuclei: blue). (f) Immunofluorescence staining of samples in group #4 on day 24 (F-actin: green, OPN: red, HUVEC: white, cell nuclei: blue). (g–i) H&E, Masson's Trichrome, and Alizarin Red staining of samples in group #4 on day 17. (j–n) Quantification of VEGF (j), BMP-2 (k), ALP (l), and OCN (m), and OPN (n) expression by ELISA on day 24. Scale bars in (c,e,f) 100 μm and (g–i) 50 μm (subset: 20 μm). Student's *t*-test was used to analyze the data; "*" indicates statistical significance (*p < 0.05; **p < 0.01; ***p < 0.005; ****p < 0.001), and ns indicates no significance.

endothelial cell growth medium-2 (EGM-2) mixed medium. The cell density of GFP-HUVECs was the same for groups #1 and #2; the cell ratio of dispersive MSCs to HUVECs in group #1 was set at 2:1, as was the cell ratio of prevascularized spheroids in groups #3 and #4. The only difference between group #2 and group #4 was whether the spheroids were prevascularized. For group #3 and group #4, the only difference was whether the HUVECs were included in the continuous phase of the GAP bioink, i.e., the ECM solution.

GFP-HUVECs were initially maintained in the interstitial space between the aggregates but rapidly organized into tubular vessel-like network structures on day 1 for both group #2 and group #4 (Figure 3b). However, most GFP-HUVECs remained round, and only a few capillaries formed on day 3 for group #1 (Figure 3c), suggesting that MSC spheroids

https://doi.org/10.1021/acsami.3c08550
ACS Appl. Mater. Interfaces XXXX, XXX, XXX−XXX

significantly promoted vascularization. In groups 3 and #4, the preformed microvessels quickly grew out of the spheroids into the surrounding ECM gel on day 3, indicating that they were stable and exhibited angiogenic activity. On day 3 in group #4, the microvessels from these prevascularized spheroids formed connections with the surrounding microvessels in the ECM gel (Figure S8). Additionally, on day 7 for group #3, prevascularized spheroids developed an interconnected vessel network through angiogenic sprouting (Figures 3d, S9). A quantitative analysis of vessel formation (Figure 3e,f) revealed greater capillary-like formation in GAP bioink (group #3) than in DCL bioink (group #1) as well as upregulated expression levels of angiogenesis-related genes, including transforming growth factor β 1 (Figure 3g), vascular endothelial growth factor (VEGF) (Figure 3h), and matrix metallopeptidase 2, on day 7 (Figure 3i). As group #2 had a significantly longer tube length than group #1, mesenchymal condensation accelerated the angiogenic process; however, the differences were minimal by day 7. HUVEC inclusion in the continuous phase (group #4 vs group #3) and prevascularization of MSC spheroids in GAP bioink (group #4 vs group #2) significantly promoted the angiogenic capabilities of HUVECs on day 3; however, no significant changes were observed on day 7. These results indicate that GAP bioinks with prevascularized spheroids are more effective in accelerating blood vessel formation than GAP bioinks with MSC spheroids or DCL bioinks.

Native bone is formed mainly through intramembranous ossification and endochondral ossification, which are initiated by the condensation of mesenchymal cells and coincide with the evolution of capillaries.[45] To evaluate the osteogenic differentiation potential, GAP bioinks were cultured in osteogenic conditions by comparing them with conventional DCL bioinks consisting of MSC-only or MSC/HUVECs (Figure 4a). The 3D bioprinted structures were first cultured with GM/EGM-2 for 3 days to promote the proliferation of MSCs and vascularization of HUVECs and then replaced with osteogenic medium (OM) for 21 days to induce osteogenesis (Figure 4b). As a result of osteogenic culture conditions, the capillaries formed by endothelial cells in the DCL bioink (group #2) quickly degenerated (Figure S10), which is consistent with previous reports.[46,47] However, the capillaries formed by prevascularized spheroids in the GAP bioink were much more robust on day 7 (Figure 4c,d). To confirm the expression profiles of osteogenic markers, we determined the early osteogenic marker Runx2 and late osteogenic marker osteopontin (OPN) by immunostaining on day 17 (Figure 4e) and day 24 (Figures 4f; S11), respectively. Moreover, HUVECs were labeled with green fluorescence to monitor capillary dynamics. As osteogenesis and vascularization are tightly coupled, the GAP bioink with intact capillaries exhibited more significant expression of Runx2 and OPN after 2−3 weeks of osteogenic culture. Using H&E (Figures 4g, S12a) and Masson's trichrome staining (Figures 4h, S12b), we found that the newly formed osteoid tissues from the GAP bioink groups were rich in collagen. In contrast, the DCL bioink groups were primarily stained red, indicating a lack of active bone regeneration. Alizarin Red staining (Figures 4i, S12c) revealed higher calcium deposition in the GAP bioink containing prevascularized spheroids, which was further confirmed by SEM images of hydroxyapatite crystals (Figure S13). During bone development in vivo, MSCs stimulate blood vessel growth by secreting angiogenic growth factors such as VEGF,[48] which in turn promotes osteoblast differentiation and matrix mineralization.[49] Bone morphogenetic protein-2 (BMP-2) has been found to be involved in bone formation and mineralization, while VEGF is essential for the formation of new blood vessels. The increased secretion of both BMP-2 and VEGF (Figure 4j,k) on day 24 indicates that the GAP bioink is more effective in inducing bone and blood vessel formation. The secretion of early (alkaline phosphatase: ALP) and late osteogenic markers (osteocalcin: OCN; OPN) (Figure 4l−n) on day 24 indicated a superior osteogenesis capability of the GAP bioink by combining the angiogenic niche and osteogenic niche, further confirmed by upregulated expression levels of osteogenesis-related genes, including ALP, Runx2, and SOST (i.e., Sclerostin) (Figure S14). Together, we printed highly vascularized bone tissues by capitalizing on the osteogenic and vasculogenic properties of the GAP bioink.

3. CONCLUSIONS

The convergence of the bioprinting technique and cellular self-organization offers a promising avenue for fabricating complex functional tissues with a close to physiological cell density, microarchitecture, and function. In this study, the GAP bioink has been shown to offer excellent self-organization and angiogenic capabilities, where prevascularized aggregates (e.g., spheroids and organoids) are used as primary vascularization units for regenerative applications. The GAP bioink can be printed into complex tissue constructs with high cell density (~1.5×10^8 cells/cm^3), viability (~80%), and shape fidelity. By recapitulating the bone developmental process, we were able to fabricate vascularized bone tissues that exhibited a higher degree of angiogenesis and osteogenesis than those of conventional DCL bioinks. Perfusable vascular networks are required to satisfy the metabolic demand of thick bone tissues with a high cell density. Therefore, our ongoing work focuses on printing perfusable vascular networks within dense tissue constructs by integrating GAP bioink with advanced bioprinting strategies.

4. EXPERIMENTAL SECTION

4.1. Materials. Gelatin (type A, 300 bloom from porcine skin), fibrinogen, and thrombin from bovine plasma were purchased from Sigma-Aldrich. GelMA hydrogels with a methacrylate degree of 30% were purchased from EFL Inc., Suzhou, China. Red- and green-fluorescence-conjugated GelMA hydrogels were used to visualize the bioprinted constructs. Primary HUVECs and adipose-derived MSCs were purchased from Zhong Qiao Biotechnology Co., Ltd., Shanghai.

4.2. Cell Culture. Primary HUVECs were cultured in EGM-2 BulletKits (CC-3162, Lonza). The culture plates were precoated with 50 μg/mL fibronectin (Corning Inc., US). The MSCs were cultured in GM consisting of high-glucose Dulbecco's modified Eagle medium (DMEM) with 10% v/v fetal bovine serum (FBS, Bioind) and 1% v/v penicillin/streptomycin (P/S, Life Technologies). Primary HUVECs and MSCs at passages 3−6 were used in the experiments. The MSCs/HUVECs were cocultured in a mixture of EGM-2 and GM at a 1:1 ratio (GM/EGM-2). Osteogenic differentiation was induced in OM comprising low-glucose DMEM supplemented with 10% v/v FBS, 1% v/v P/S, 100 nM dexamethasone, 10 mM sodium-β-glycerophosphate, and 0.05 mM ascorbic acid-2-phosphate.

4.3. Retroviral Transduction. For live imaging, the cells were infected with retroviruses expressing GFP or RFP by strictly following the instructions from the manufacturer (Hanbio, Shanghai, China). Briefly, cells at 60% confluence were washed gently with PBS and treated with a virus-containing medium with polybrene (5 μg/mL). After 24 h, the culture medium was replaced with fresh medium. Most cells started to express RFP or GFP 48 h after transfection. RFP- or GFP-expressing cells were harvested after 3 days of viral infection.

https://doi.org/10.1021/acsami.3c08550
ACS Appl. Mater. Interfaces XXXX, XXX, XXX−XXX

4.4. Massive Generation of Spheroids. Spheroids were formed by suspending cells into microwells (Aggrewell 400; StemCell Technologies) at a density of 100−1000 cells/microwell, as described in the previous report.[50] Each 6-well Aggrewell plate has approximately 300 microwells. Thus, the number of cells collected in each microwell can be estimated by dividing the total number of cells by the number of microwells. Single cells were transferred to Aggrewell plates and centrifuged to facilitate aggregation. After 72 h, spheroids were transferred to rotary orbital suspension culture (at a speed of 60−65 rpm) and maintained for further culture and characterization. The diameters and roundness of the spheroids were analyzed using ImageJ software (NIH).

4.5. Bioink Preparation. GAP bioink was prepared by mixing spheroids with Gelbrin solution. A 5 wt % Gelbrin solution was prepared by mixing 10 wt % GelMA and 10 mg/mL fibrinogen stock solution at a volume ratio of 1:1. The spheroids were harvested manually using a pipet with wide-bore tips. The spheroids were collected from 5−10 plates at a time and transferred into a single 15 mL centrifuge tube. Upon collection, the spheroids were allowed to settle by centrifugation at 1000 rpm for 3 min. After the supernatant was aspirated, the volume (x mL) of compacted spheroids was estimated visually by pipetting known volumes of PBS solution into a second tube to match the height of the pellet in the spheroid-laden tube. We subsequently washed compacted spheroids in a 3× volume of Gelbrin solution. After mixing with the wide-bore pipet, the 15 mL tube was centrifuged at 1000 rpm for 3 min. Next, the Gelbrin supernatant was aspirated and replaced with 2× volume of Gelbrin solution. The mixed spheroids were transferred to a syringe and further compacted before printing. The final volume of the mixed spheroids was estimated as y mL. The volume fraction of spheroids could be calculated by x/y. As a control group, DCL bioink containing cell-laden Gelbrin solution (5 wt %) was used at a density of 7.5×10^6 cells/cm^3. As with prevascularized spheroids, the cell ratio of dispersive MSCs to HUVECs was set at 2:1.

4.6. 3D Bioprinting. 3D bioprinting was performed using a commercial 3D bioprinter (SunP Inc., China). All digital models were converted to STL format files and imported into slicing software to generate G-Code instructions. The printer chamber was UV-sterilized for 60 min before printing. GAP bioinks were loaded into a 1 mL syringe (BD) and centrifuged at 1000 rpm for 10 s to remove air bubbles. For 3D printing of the GAP bioink, a printing speed of 5 mm/s and an extrusion rate of 1.8 mm^3/s were used. Upon print completion, the Petri dish containing the printed construct was immediately exposed to visible light irradiation (405 nm, ∼10 mW/cm^2) for 60 s, followed by enzymatic cross-linking with thrombin solution (10 U/mL). For embedded printing, we used a Carbopol-based suspension medium (SunP Inc., China) consisting of poly(acrylic acid)-based microgels with diameters of ∼7 μm. After printing and photo-cross-linking, the Carbopol-based suspension medium was removed by repeated rinsing with PBS solution. The cell density of the printed structures was quantified by dissociating them into single cells, followed by automatic counting using a cell counter (Countstar, China).

4.7. Morphological Characterization. The microstructure of the 3D-printed constructs was observed by using SEM. The samples were first fixed at room temperature in formalin for 1 h and washed with ultrapure water, followed by dehydration in increasing ethanol gradients and infiltration with tertiary butanol. The samples were freeze-dried, sputter-coated with gold (thickness: 20 nm), and imaged with a Zeiss Auriga SEM system at 15 kV.

4.8. Rheological Characterization. The rheological properties of Gelbrin and GAP bioinks were measured by using a rheometer (MCR301, Anton Paar) with a 25 mm diameter cone plate geometry (gap: 750 μm). Shear rate sweeps ranging from 0.1 to 100 s^{-1} were performed to evaluate the shear-thinning property. Strain sweeps ranging from 0.1 to 1000% (frequency: 1 Hz) were performed to evaluate the strain-yielding property. The storage (G') and loss moduli (G'') were measured with alternating low (1%) and high (300%) strains (1 Hz, 100 s) to evaluate the self-healing property. Temperature sweeps ranging from 4 to 37 °C (strain: 0.1%, frequency: 1 Hz) were performed to evaluate the temperature responsiveness.

4.9. Mechanical Characterization. A uniaxial compression test was conducted to determine the mechanical properties of the Gelbrin and GAP bioinks. With the use of a mechanical test instrument (Bose ElectroForce 3200, Bose Corp.), cylindrical samples (diameter of 8 mm, height of 5 mm) were loaded and compressed until rupture at a rate of 0.1 mm/s. For the calculation of the elastic modulus, the elastic part (0 to 20% strain) of the stress−strain curve was selected. At least three samples were tested for each condition.

4.10. Cell Viability. Cell viability was assessed by using a Calcein-AM/PI Double Staining Kit (Dojindo Molecular Technologies). Briefly, the samples were incubated with 2 mM calcein AM and 4.5 mM propidium iodide at 37 °C for 30 min and then visualized by using a laser-scanning confocal microscope (FV3000, Olympus). Using ImageJ software, we determined cell viability by dividing live cell numbers by total cell numbers.

4.11. Histological and Immunofluorescent Analysis. After 3 weeks of osteogenic culture, 3D bioprinted constructs were fixed in 10% formalin for 24 h at 4 °C before being transferred to 70% ethanol. Following paraffin processing, 10 μm sections were cut using a microtome (Leica Microsystems Inc., USA) and stained with hematoxylin and eosin (H&E), Alizarin Red, and Masson's trichrome. For immunofluorescence staining, all sections or samples were permeabilized with 0.1% Triton X-100 (Sigma) and blocked in 10% bovine serum albumin in PBST solution (0.1% Tween in PBS) for 1 h before incubation with primary antibodies at 4 °C overnight. The primary antibodies used in prevascularized spheroids were as follows: CD44 (1:500, ab6124, Abcam) and CD31 (1:500, ab32457, Abcam). The primary antibodies used in the osteogenic samples were as follows: Runx2 (1:200, ab215955, Abcam) and OPN (1:200, ab63856, Abcam). Following washing with PBS, the samples were incubated with fluorescein-conjugated secondary antibodies of Alexa Fluor 488 goat antimouse (1:300, JAC-115-545-003, Jackson) and Alexa Fluor 594 goat antirabbit (1:300, JAC-111-585-144, Jackson) at room temperature for 2 h and counterstained with 4′,6-diamidino-2-phenylindole (1:1000, Beyotime) to visualize cell nuclei. Actin filaments (green) were stained with CytoPainter Phalloidin-iFluor 488 reagent (1:100, ab176753, Abcam). Nuclei were stained with Hoechst 33258 (Dojindo, Japan) at a 1/1000 dilution in PBS. Stained samples were observed under a confocal microscope. The total and mean tube lengths of capillaries were quantified by ImageJ software with the Angiogenesis Analyzer plugin tool.

4.12. ELISA Quantification. The expression of human BMP-2 and VEGF in the culture supernatants was quantified using BMP-2 (QZ-10621) and VEGF (QZ-10748) ELISA kits according to the instructions from Jiubang Biotechnology, Quanzhou, China. Similarly, the expression of ALP, OPN, and OCN was also detected by using ALP (QZ-10660), OPN (QZ-10628), and OCN (QZ-10626) ELISA kits. The expression level was further normalized to the cell number.

4.13. Quantitative Real-Time Polymerase Chain Reaction. Samples were homogenized to obtain mRNA using TRIzol (Invitrogen), which was reverse-transcribed into complementary DNA (cDNA) using a PrimeScript RT Reagent Kit (TaKaRa, RR037A). Quantitative real-time polymerase chain reaction was performed on a CFX96 real-time system (Bio-Rad, USA) using a mixture of the obtained cDNA and TB Green Premix Ex Taq (Tli RNaseH Plus) according to the manufacturer's instructions. The expression level of target genes was normalized to that of glyceraldehyde-3-phosphate dehydrogenase (GAPDH) by the $\Delta\Delta Ct$ method.

4.14. Statistical Analysis. All of the experimental statistical data were analyzed from at least three parallel samples and expressed as the mean ± standard deviation. Statistical analysis between the two groups was performed using an unpaired two-tailed Student's t-test with GraphPad Prism software. Statistically significant differences between multiple experimental groups were determined by a one-way analysis of variance (ANOVA). Post hoc pairwise analysis was performed with the Tukey's honestly significant difference test. The

https://doi.org/10.1021/acsami.3c08550
ACS Appl. Mater. Interfaces XXXX, XXX, XXX−XXX

differences were considered statistically significant if the p value was below 0.05 (*).

■ ASSOCIATED CONTENT

Supporting Information

The Supporting Information is available free of charge on the ACS Publications Web site at DOI: (input by editor). Figures S1−S14 (PDF) The Supporting Information is available free of charge at https://pubs.acs.org/doi/10.1021/acsami.3c08550.

In situ monitoring of HUVEC spheroid formation; immunostaining of MSC/HUVEC spheroids; formation of capillary networks within the fibrin hydrogel on day 7; preparation process for GAP bioink; cell viabilities and densities of spheroids at various volume fractions; rheological characterization of Gelbrin; mechanical characterization of printed cylinders using Gelbrin and Gap bioink; capillary formation by HUVEC self-assembly in Group #4; confocal images of samples in Group #3 on day 7; representative confocal images of samples on day 7; immunofluorescence staining on day 24; H&E, Masson's trichrome, and Alizarin Red staining on day 17; hydroxyapatite deposition within the printed structures using the GAP bioink by SEM micrographs and EDS spectra on day 24; and osteogenic-related gene expression on day 24 (PDF)

■ AUTHOR INFORMATION

Corresponding Author

Zhuo Xiong − *Biomanufacturing Center, Department of Mechanical Engineering, Tsinghua University, Beijing 100084, P. R. China; Biomanufacturing and Rapid Forming Technology Key Laboratory of Beijing, Beijing 100084, P. R. China; Biomanufacturing and Engineering Living Systems" Innovation International Talents Base (111 Base), Beijing 100084, P. R. China;* orcid.org/0000-0002-9205-086X; Phone: +86-135-0111-1907; Email: xiongzhuo@tsinghua.edu.cn

Authors

Yongcong Fang − *Biomanufacturing Center, Department of Mechanical Engineering, Tsinghua University, Beijing 100084, P. R. China; Biomanufacturing and Rapid Forming Technology Key Laboratory of Beijing, Beijing 100084, P. R. China; Biomanufacturing and Engineering Living Systems" Innovation International Talents Base (111 Base), Beijing 100084, P. R. China*

Mengke Ji − *Biomanufacturing Center, Department of Mechanical Engineering, Tsinghua University, Beijing 100084, P. R. China; Biomanufacturing and Rapid Forming Technology Key Laboratory of Beijing, Beijing 100084, P. R. China; Biomanufacturing and Engineering Living Systems" Innovation International Talents Base (111 Base), Beijing 100084, P. R. China*

Bingyan Wu − *Biomanufacturing Center, Department of Mechanical Engineering, Tsinghua University, Beijing 100084, P. R. China; Biomanufacturing and Rapid Forming Technology Key Laboratory of Beijing, Beijing 100084, P. R. China; Biomanufacturing and Engineering Living Systems" Innovation International Talents Base (111 Base), Beijing 100084, P. R. China*

Xinxin Xu − *Senior Department of General Surgery, the First Medical Center, Chinese PLA General Hospital, Beijing 100853, P. R. China*

Ge Wang − *Biomanufacturing Center, Department of Mechanical Engineering, Tsinghua University, Beijing 100084, P. R. China; Biomanufacturing and Rapid Forming Technology Key Laboratory of Beijing, Beijing 100084, P. R. China; Biomanufacturing and Engineering Living Systems" Innovation International Talents Base (111 Base), Beijing 100084, P. R. China*

Yanmei Zhang − *Biomanufacturing Center, Department of Mechanical Engineering, Tsinghua University, Beijing 100084, P. R. China; Biomanufacturing and Rapid Forming Technology Key Laboratory of Beijing, Beijing 100084, P. R. China; Biomanufacturing and Engineering Living Systems" Innovation International Talents Base (111 Base), Beijing 100084, P. R. China*

Yingkai Xia − *Biomanufacturing Center, Department of Mechanical Engineering, Tsinghua University, Beijing 100084, P. R. China; Biomanufacturing and Rapid Forming Technology Key Laboratory of Beijing, Beijing 100084, P. R. China; Biomanufacturing and Engineering Living Systems" Innovation International Talents Base (111 Base), Beijing 100084, P. R. China*

Zhe Li − *Biomanufacturing Center, Department of Mechanical Engineering, Tsinghua University, Beijing 100084, P. R. China; Biomanufacturing and Rapid Forming Technology Key Laboratory of Beijing, Beijing 100084, P. R. China; Biomanufacturing and Engineering Living Systems" Innovation International Talents Base (111 Base), Beijing 100084, P. R. China*

Ting Zhang − *Biomanufacturing Center, Department of Mechanical Engineering, Tsinghua University, Beijing 100084, P. R. China; Biomanufacturing and Rapid Forming Technology Key Laboratory of Beijing, Beijing 100084, P. R. China; Biomanufacturing and Engineering Living Systems" Innovation International Talents Base (111 Base), Beijing 100084, P. R. China*

Wei Sun − *Biomanufacturing Center, Department of Mechanical Engineering, Tsinghua University, Beijing 100084, P. R. China; Biomanufacturing and Rapid Forming Technology Key Laboratory of Beijing, Beijing 100084, P. R. China; Biomanufacturing and Engineering Living Systems" Innovation International Talents Base (111 Base), Beijing 100084, P. R. China; Department of Mechanical Engineering, Drexel University, Philadelphia, Pennsylvania 19104, United States of America*

Complete contact information is available at: https://pubs.acs.org/10.1021/acsami.3c08550

Author Contributions

Y.C.F and Z.X. conceived and designed the study. Y.C.F performed the 3D printing and biological experiments. M.K.J. performed the cell culture and spheroid generation. B.Y.W. performed the mechanical analysis. X.X.X. and Y.M.Z performed the H&E, Alizarin Red, and Masson's Trichrome staining. G.W. performed the SEM characterization. Y.K.X. and Z.L. helped on the data collection and analysis. Y.C.F wrote the original manuscript. T.Z., W.S., and Z.X. revised the prepared manuscript.

Notes

The authors declare no competing financial interest.

https://doi.org/10.1021/acsami.3c08550
ACS Appl. Mater. Interfaces XXXX, XXX, XXX−XXX

■ ACKNOWLEDGMENTS

We gratefully acknowledge the funding support from the National Natural Science Foundation of China (grant no. U21A20394), New Faculty Start-up Funding of Tsinghua University (53330200321), National Key Research and Development Program of China (2018YFA0703004), and China Postdoctoral Science Foundation (2021TQ0184). We thank Jingjing Wang and Yue Sun at the Cell Biology Facility, Center of Biomedical Analysis, Tsinghua University, for their help with confocal microscopy.

■ REFERENCES

(1) Fang, Y.; Guo, Y.; Liu, T.; Xu, R.; Mao, S.; Mo, X.; Zhang, T.; Ouyang, L.; Xiong, Z.; Sun, W. Advances in 3D Bioprinting. *Chin. J. Mech. Eng.* **2022**, *1*, 100011.

(2) Brassard, J. A.; Nikolaev, M.; Hübscher, T.; Hofer, M.; Lutolf, M. P. Recapitulating Macro-Scale Tissue Self-Organization through Organoid Bioprinting. *Nat. Mater.* **2021**, *20*, 22−29.

(3) Gadjanski, I.; Spiller, K.; Vunjak-Novakovic, G. Time-Dependent Processes in Stem Cell-Based Tissue Engineering of Articular Cartilage. *Stem Cell Rev. Rep.* **2012**, *8*, 863−881.

(4) Laurent, J.; Blin, G.; Chatelain, F.; Vanneaux, V.; Fuchs, A.; Larghero, J.; Théry, M. Convergence of Microengineering and Cellular Self-Organization towards Functional Tissue Manufacturing. *Nat. Biomed. Eng.* **2017**, *1*, 939−956.

(5) Shinozawa, T.; Yoshikawa, H. Y.; Takebe, T. Reverse Engineering Liver Buds through Self-Driven Condensation and Organization towards Medical Application. *Dev. Biol.* **2016**, *420*, 221−229.

(6) Kim, J.; Adachi, T. Cell Condensation Triggers the Differentiation of Osteoblast Precursor Cells to Osteocyte-Like Cells. *Front. Bioeng. Biotechnol.* **2019**, *7*, 288.

(7) Kim, J.; Adachi, T. Cell-fate Decision of Mesenchymal Stem Cells toward Osteocyte Differentiation Is Committed by Spheroid Culture. *Sci. Rep.* **2021**, *11*, 13204.

(8) Liu, Y.; Dabrowska, C.; Mavousian, A.; Strauss, B.; Meng, F.; Mazzaglia, C.; Ouaras, K.; Macintosh, C.; Terentjev, E.; Lee, J. H.; et al. Bio-assembling Macro-Scale, Lumenized Airway Tubes of Defined Shape via Multi-Organoid Patterning and Fusion. *Adv. Sci.* **2021**, *8*, 2003332.

(9) Kim, W.; Gwon, Y.; Park, S.; Kim, H.; Kim, J. Therapeutic Strategies of Three-Dimensional Stem Cell Spheroids and Organoids for Tissue Repair and Regeneration. *Bioact. Mater.* **2023**, *19*, 50−74.

(10) Tan, N.; Yang, Y. Y. Building Blocks to The Future of Regenerative Medicine: Organoid bioprinting. *Matter* **2021**, *4*, 2659−2661.

(11) Moldovan, N. I.; Hibino, N.; Nakayama, K. Principles of the *Kenzan* Method for Robotic Cell Spheroid-Based Three-Dimensional Bioprinting. *Tissue Eng. B Rev.* **2017**, *23*, 237−244.

(12) Ayan, B.; Heo, D. N.; Zhang, Z.; Dey, M.; Povilianskas, A.; Drapaca, C.; Ozbolat, I. T. Aspiration-assisted Bioprinting for Precise Positioning of Biologics. *Sci. Adv.* **2020**, *6*, w5111.

(13) Daly, A. C.; Davidson, M. D.; Burdick, J. A. 3D Bioprinting of High Cell-Density Heterogeneous Tissue Models through Spheroid Fusion within Self-Healing Hydrogels. *Nat. Commun.* **2021**, *12*, 753.

(14) Vrij, E.; Rouwkema, J.; LaPointe, V.; van Blitterswijk, C.; Truckenmüller, R.; Rivron, N. Directed Assembly and Development of Material-Free Tissues with Complex Architectures. *Adv. Mater.* **2016**, *28*, 4032−4039.

(15) Jeger Madiot, N.; Arakelian, L.; Setterblad, N.; Bruneval, P.; Hoyos, M.; Larghero, J.; Aider, J. L. Author Correction: Self-organization and Culture of Mesenchymal Stem Cell Spheroids in Acoustic Levitation. *Sci. Rep.* **2021**, *11*, 12936.

(16) Parfenov, V. A.; Khesuani, Y. D.; Petrov, S. V.; Karalkin, P. A.; Koudan, E. V.; Nezhurina, E. K.; Pereira, F. D.; Krokhmal, A. A.; Gryadunova, A. A.; Bulanova, E. A.; et al. Magnetic Levitational Bioassembly of 3D Tissue Construct in Space. *Sci. Adv.* **2020**, *6*, a4174.

(17) Sousa, A. R.; Martins-Cruz, C.; Oliveira, M. B.; Mano, J. F. One-Step Rapid Fabrication of Cell-Only Living Fibers. *Adv. Mater.* **2020**, *32*, No. e1906305.

(18) Ren, Y.; Yang, X.; Ma, Z.; Sun, X.; Zhang, Y.; Li, W.; Yang, H.; Qiang, L.; Yang, Z.; Liu, Y.; et al. Developments and Opportunities for 3D Bioprinted Organoids. *Int. J. Bioprint.* **1970**, *7*, 364.

(19) De Moor, L.; Merovci, I.; Baetens, S.; Verstraeten, J.; Kowalska, P.; Krysko, D. V.; De Vos, W. H.; Declercq, H. High-throughput Fabrication of Vascularized Spheroids for Bioprinting. *Biofabrication* **2018**, *10*, 035009.

(20) Goulart, E.; de Caires-Junior, L. C.; Telles-Silva, K. A.; Araujo, B. H. S.; Rocco, S. A.; Sforca, M.; de Sousa, I. L.; Kobayashi, G. S.; Musso, C. M.; Assoni, A. F.; et al. 3D Bioprinting of Liver Spheroids derived from Human Induced Pluripotent Stem Cells Sustain Liver Function and Viability in Vitro. *Biofabrication* **2019**, *12*, 015010.

(21) De Moor, L.; Fernandez, S.; Vercruysse, C.; Tytgat, L.; Asadian, M.; De Geyter, N.; Van Vlierberghe, S.; Dubruel, P.; Declercq, H. Hybrid Bioprinting of Chondrogenically Induced Human Mesenchymal Stem Cell Spheroids. *Front. Bioeng. Biotechnol.* **2020**, *8*, 484.

(22) Lavrador, P.; Gaspar, V. M.; Mano, J. F. Engineering Mammalian Living Materials towards Clinically Relevant Therapeutics. *Ebiomedicine* **2021**, *74*, 103717.

(23) Skylar-Scott, M. A.; Uzel, S. G. M.; Nam, L. L.; Ahrens, J. H.; Truby, R. L.; Damaraju, S.; Lewis, J. A. Biomanufacturing of Organ-Specific Tissues with High Cellular Density and Embedded Vascular Channels. *Sci. Adv.* **2019**, *5*, w2459.

(24) Greco Song, H. H.; Rumma, R. T.; Ozaki, C. K.; Edelman, E. R.; Chen, C. S. Vascular Tissue Engineering: Progress, Challenges, and Clinical Promise. *Cell Stem Cell* **2018**, *22*, 608.

(25) Fleischer, S.; Tavakol, D. N.; Vunjak Novakovic, G. From Arteries to Capillaries: Approaches to Engineering Human Vasculature. *Adv. Funct. Mater.* **2020**, *30*, 1910811.

(26) Laschke, M. W.; Menger, M. D. Spheroids as Vascularization Units: From Angiogenesis Research to Tissue Engineering Applications. *Biotechnol. Adv.* **2017**, *35*, 782−791.

(27) De Moor, L.; Smet, J.; Plovyt, M.; Bekaert, B.; Vercruysse, C.; Asadian, M.; De Geyter, N.; Van Vlierberghe, S.; Dubruel, P.; Declercq, H. Engineering microvasculature by 3D bioprinting of prevascularized spheroids in photo-crosslinkable gelatin. *Biofabrication* **2021**, *13*, 045021.

(28) Lee, J.; Ung, A.; Kim, H.; Lee, K.; Cho, H.; Bandaru, P.; Ahadian, S.; Dokmeci, M. R.; Khademhosseini, A. Engineering Liver Microtissues to Study the Fusion of HepG2 with Mesenchymal Stem Cells and Invasive Potential of Fused Cells. *Biofabrication* **2021**, *14*, 014104.

(29) Dahlmann, J.; Kensah, G.; Kempf, H.; Skvorc, D.; Gawol, A.; Elliott, D. A.; Dräger, G.; Zweigerdt, R.; Martin, U.; Gruh, I. The Use of Agarose Microwells for Scalable Embryoid Body Formation and Cardiac Differentiation of Human and Murine Pluripotent Stem Cells. *Biomaterials* **2013**, *34*, 2463−2471.

(30) Chen, Y.; Lin, R.; Qi, H.; Yang, Y.; Bae, H.; Melero-Martin, J. M.; Khademhosseini, A. Functional Human Vascular Network Generated in Photocrosslinkable Gelatin Methacrylate Hydrogels. *Adv. Funct. Mater.* **2012**, *22*, 2027−2039.

(31) Ma, J.; Yang, F.; Both, S. K.; Prins, H.; Helder, M. N.; Pan, J.; Cui, F.; Jansen, J. A.; van den Beucken, J. J. In Vitro and in Vivo Angiogenic Capacity of BM-MSCs/HUVECs and AT-MSCs/HUVECs Cocultures. *Biofabrication* **2014**, *6*, 015005.

(32) Mao, M.; Qu, X.; Zhang, Y.; Gu, B.; Li, C.; Liu, R.; Li, X.; Zhu, H.; He, J.; Li, D. Leaf-Venation-Directed Cellular Alignment for Macroscale Cardiac Constructs with Tissue-Like Functionalities. *Nat. Commun.* **2023**, *14*, 2077.

(33) Murphy, K. C.; Whitehead, J.; Zhou, D.; Ho, S. S.; Leach, J. K. Engineering Fibrin Hydrogels to Promote the Wound Healing Potential of Mesenchymal Stem Cell Spheroids. *Acta Biomater.* **2017**, *64*, 176−186.

https://doi.org/10.1021/acsami.3c08550
ACS Appl. Mater. Interfaces XXXX, XXX, XXX−XXX

(34) Fang, Y.; Guo, Y.; Ji, M.; Li, B.; Guo, Y.; Zhu, J.; Zhang, T.; Xiong, Z. 3D Printing of Cell-Laden Microgel-Based Biphasic Bioink with Heterogeneous Microenvironment for Biomedical Applications. *Adv. Funct. Mater.* **2022**, *32*, 2109810.
(35) Jia, S.; Wang, J.; Zhang, T.; Pan, W.; Li, Z.; He, X.; Yang, C.; Wu, Q.; Sun, W.; Xiong, Z.; et al. Multilayered Scaffold with a Compact Interfacial Layer Enhances Osteochondral Defect Repair. *ACS Appl. Mater. Interfaces* **2018**, *10*, 20296−20305.
(36) Xin, S.; Deo, K. A.; Dai, J.; Pandian, N. K. R.; Chimene, D.; Moebius, R. M.; Jain, A.; Han, A.; Gaharwar, A. K.; Alge, D. L. Generalizing Hydrogel Microparticles into a New Class of Bioinks for Extrusion Bioprinting. *Sci. Adv.* **2021**, *7*, k3087.
(37) Grosskopf, A. K.; Truby, R. L.; Kim, H.; Perazzo, A.; Lewis, J. A.; Stone, H. A. Viscoplastic Matrix Materials for Embedded 3D Printing. *ACS Appl. Mater. Interfaces* **2018**, *10*, 23353−23361.
(38) Kang, H.; Lee, S. J.; Ko, I. K.; Kengla, C.; Yoo, J. J.; Atala, A. A 3D Bioprinting System to Produce Human-Scale Tissue Constructs with Structural Integrity. *Nat. Biotechnol.* **2016**, *34*, 312−319.
(39) Pati, F.; Jang, J.; Ha, D.; Won Kim, S.; Rhie, J.; Shim, J.; Kim, D.; Cho, D. Printing Three-Dimensional Tissue Analogues with Decellularized Extracellular Matrix Bioink. *Nat. Commun.* **2014**, *5*, 3935.
(40) Chae, S.; Lee, S.; Choi, Y.; Hong, D. H.; Gao, G.; Wang, J. H.; Cho, D. 3D Cell-printing of Biocompatible and Functional Meniscus Constructs Using Meniscus-Derived Bioink. *Biomaterials* **2021**, *267*, 120466.
(41) Sun, Y.; Zhang, Y.; Wu, Q.; Gao, F.; Wei, Y.; Ma, Y.; Jiang, W.; Dai, K. 3D-bioprinting Ready-To-Implant Anisotropic Menisci Recapitulate Healthy Meniscus Phenotype and Prevent Secondary Joint Degeneration. *Theranostics* **2021**, *11*, 5160−5173.
(42) Sun, Y.; You, Y.; Jiang, W.; Wu, Q.; Wang, B.; Dai, K. Generating Ready-To-Implant Anisotropic Menisci by 3D-Bioprinting Protein-Releasing Cell-Laden Hydrogel-Polymer Composite Scaffold. *Appl. Mater. Today* **2020**, *18*, 100469.
(43) Lin, S.; Yang, G.; Jiang, F.; Zhou, M.; Yin, S.; Tang, Y.; Tang, T.; Zhang, Z.; Zhang, W.; Jiang, X. A Magnesium-Enriched 3D Culture System that Mimics the Bone Development Microenvironment for Vascularized Bone Regeneration. *Adv. Sci.* **2019**, *6*, 1900209.
(44) Zhou, X.; Qian, Y.; Chen, L.; Li, T.; Sun, X.; Ma, X.; Wang, J.; He, C. Flowerbed-Inspired Biomimetic Scaffold with Rapid Internal Tissue Infiltration and Vascularization Capacity for Bone Repair. *ACS Nano* **2023**, *17*, 5140−5156.
(45) McDermott, A. M.; Herberg, S.; Mason, D. E.; Collins, J. M.; Pearson, H. B.; Dawahare, J. H.; Tang, R.; Patwa, A. N.; Grinstaff, M. W.; Kelly, D. J.; et al. Recapitulating Bone Development through Engineered Mesenchymal Condensations and Mechanical Cues for Tissue Regeneration. *Sci. Transl. Med.* **2019**, *11*, No. eaav7756.
(46) Kageyama, T.; Akieda, H.; Sonoyama, Y.; Sato, K.; Yoshikawa, H.; Isono, H.; Hirota, M.; Kitajima, H.; Chun, Y.; Maruo, S.; et al. Bone beads enveloped with vascular endothelial cells for bone regenerative medicine. *Acta Biomater.* **2023**, *165*, 168−179.
(47) Qiu, P.; Li, M.; Chen, K.; Fang, B.; Chen, P.; Tang, Z.; Lin, X.; Fan, S. Periosteal matrix-derived hydrogel promotes bone repair through an early immune regulation coupled with enhanced angio- and osteogenesis. *Biomaterials* **2020**, *227*, 119552.
(48) Hasani-Sadrabadi, M. M.; Sarrion, P.; Pouraghaei, S.; Chau, Y.; Ansari, S.; Li, S.; Aghaloo, T.; Moshaverinia, A. An Engineered Cell-Laden Adhesive Hydrogel Promotes Craniofacial Bone Tissue Regeneration in Rats. *Sci. Transl. Med.* **2020**, *12*, 1.
(49) Zhu, G.; Zhang, T.; Chen, M.; Yao, K.; Huang, X.; Zhang, B.; Li, Y.; Liu, J.; Wang, Y.; Zhao, Z. Bone Physiological Microenvironment and Healing Mechanism: Basis for Future Bone-Tissue Engineering Scaffolds. *Bioact. Mater.* **2021**, *6*, 4110−4140.
(50) Razian, G.; Yu, Y.; Ungrin, M. Production of Large Numbers of Size-controlled Tumor Spheroids Using Microwell Plates. *J. Visualized Exp.* **2013**, *81*, No. e50665.

https://doi.org/10.1021/acsami.3c08550
ACS Appl. Mater. Interfaces XXXX, XXX, XXX−XXX